Science AAAS

Folding DNA into Twisted and Curved Nanoscale Shapes

Hendrik Dietz, *et al.*

Science **325**, 725 (2009);
DOI: 10.1126/science.1174251

The following resources related to this article are available online at www.sciencemag.org (this information is current as of August 6, 2009):

Updated information and services, including high-resolution figures, can be found in the online version of this article at:
http://www.sciencemag.org/cgi/content/full/325/5941/725

Supporting Online Material can be found at:
http://www.sciencemag.org/cgi/content/full/325/5941/725/DC1

This article **cites 27 articles**, 7 of which can be accessed for free:
http://www.sciencemag.org/cgi/content/full/325/5941/725#otherarticles

This article has been **cited by** 1 articles hosted by HighWire Press; see:
http://www.sciencemag.org/cgi/content/full/325/5941/725#otherarticles

This article appears in the following **subject collections**:
Chemistry
http://www.sciencemag.org/cgi/collection/chemistry

Information about obtaining **reprints** of this article or about obtaining **permission to reproduce this article** in whole or in part can be found at:
http://www.sciencemag.org/about/permissions.dtl

Science (print ISSN 0036-8075; online ISSN 1095-9203) is published weekly, except the last week in December, by the American Association for the Advancement of Science, 1200 New York Avenue NW, Washington, DC 20005. Copyright 2009 by the American Association for the Advancement of Science; all rights reserved. The title *Science* is a registered trademark of AAAS.

phase acquired by each spin under closed-path rotation, in particular the even parity of integer spins (and odd parity of half-integer spins) under 2π-rotation. This demonstration opens possibilities for using phase qudits in quantum information processing.

References and Notes

1. M. A. Nielsen, I. L. Chuang, *Quantum Computation and Quantum Information* (Cambridge Univ. Press, Cambridge, 2000).
2. A. Muthukrishnan, C. R. Stroud, *Phys. Rev. A* **62**, 052309 (2000).
3. B. Lanyon *et al.*, *Nat. Physics* **5**, 134 (2009).
4. I. Bregman, D. Aharonov, M. Ben-Or, H. S. Eisenberg, *Phys. Rev. A* **77**, 050301 (2008).
5. D. P. DiVincenzo, *Fortschr. Phys.* **48**, 771 (2000).
6. D. P. O'Leary, G. K. Brennen, S. S. Bullock, *Phys. Rev. A* **74**, 032334 (2006).
7. J. Clarke, F. K. Wilhelm, *Nature* **453**, 1031 (2008).
8. M. Steffen *et al.*, *Phys. Rev. Lett.* **97**, 050502 (2006).
9. M. Steffen *et al.*, *Science* **313**, 1423 (2006).
10. J. J. Sakurai, *Modern Quantum Mechanics* (Addison-Wesley, Reading, MA, 1994).
11. M. V. Berry, *Proc. R. Soc. Lond. A Math. Phys. Sci.* **392**, 45 (1984).
12. We worked in a rotating frame and chose the axis of rotation to be always perpendicular to the instantaneous spin direction $\langle \hat{\mathbf{S}} \rangle$, so that the dynamical phase is zero (*13*).
13. Materials and methods are available as supporting material on *Science* Online.
14. W. Pauli, *Phys. Rev.* **58**, 716 (1940).
15. I. Duck, E. C. G. Sudarshan, *Am. J. Phys.* **66**, 284 (1998).
16. H. Rauch *et al.*, *Phys. Lett.* **54A**, 425 (1975).
17. S. A. Werner, R. Colella, A. W. Overhauser, C. F. Eagen, *Phys. Rev. Lett.* **35**, 1053 (1975).
18. R. Kaiser, *Can. J. Phys.* **56**, 1321 (1978).
19. A. O. Niskanen *et al.*, *Science* **316**, 723 (2007).
20. A. Fragner *et al.*, *Science* **322**, 1357 (2008).
21. Because the global phase of a quantum system is undetectable, qudit states $|1\rangle$ and higher are used to emulate the spin, whereas the ground state $|0\rangle$ is reserved as phase reference. Hence, we emulated only up to spin-3/2, even though the 5-level qudit would map to an isolated spin-2.
22. M. Steffen, J. M. Martinis, I. L. Chuang, *Phys. Rev. B* **68**, 224518 (2003).
23. E. Lucero *et al.*, *Phys. Rev. Lett.* **100**, 247001 (2008).
24. M. Neeley *et al.*, *Phys. Rev. B* **77**, 180508 (2008).
25. G. K. Brennen, D. P. O'Leary, S. S. Bullock, *Phys. Rev. A* **71**, 052318 (2005).
26. H. Wang *et al.*, *Phys. Rev. Lett.* **101**, 240401 (2008).
27. M. Brune *et al.*, *Phys. Rev. Lett.* **101**, 240402 (2008).
28. J. M. Martinis *et al.*, *Phys. Rev. Lett.* **95**, 210503 (2005).
29. Devices were made at the UCSB Nanofabrication Facility, a part of the NSF-funded National Nanotechnology Infrastructure Network. This work was supported by the Intelligence Advanced Research Projects Activity (grant W911NF-04-1-0204) and NSF (grant CCF-0507227).

Supporting Online Material
www.sciencemag.org/cgi/content/full/325/5941/722/DC1
Materials and Methods
SOM Text
Figs. S1 and S2
References

12 March 2009; accepted 8 June 2009
10.1126/science.1173440

Folding DNA into Twisted and Curved Nanoscale Shapes

Hendrik Dietz,[1,2]* **Shawn M. Douglas,**[1,2,3] **William M. Shih**[1,2,3]†

We demonstrate the ability to engineer complex shapes that twist and curve at the nanoscale from DNA. Through programmable self-assembly, strands of DNA are directed to form a custom-shaped bundle of tightly cross-linked double helices, arrayed in parallel to their helical axes. Targeted insertions and deletions of base pairs cause the DNA bundles to develop twist of either handedness or to curve. The degree of curvature could be quantitatively controlled, and a radius of curvature as tight as 6 nanometers was achieved. We also combined multiple curved elements to build several different types of intricate nanostructures, such as a wireframe beach ball or square-toothed gears.

The sequences of DNA molecules can be engineered so that complex higher-order structures form as multiple double-helical segments connected through numerous turn regions. Programmable self-assembly based on DNA directed to branch in this way offers an attractive route to creating particular shapes on the 1- to 100-nm scale (*1*–*4*), as evidenced by its use in constructing two-dimensional (2D) crystals (*5*), nanotubes (*6*–*11*), and 3D wireframe polyhedra (*12*–*17*). More recently, oligonucleotide–"staple-strand"–assisted folding of a multiple-kilobase "scaffold strand" has been introduced as a powerful method to direct the self-assembly of custom-shaped, megadalton-scale, planar arrays of antiparallel helices connected through turn regions (*18*). In this "scaffolded–DNA-origami" method, each staple strand base pairs along part of its length with a complementary segment of the scaffold strand and then abruptly switches to base pair with another complementary scaffold segment that may be quite distant in the scaffold primary sequence. A single staple strand may pair with several scaffold-strand segments, in accordance with this switching strategy. Association with hundreds of such staple strands constrains the scaffold strand to helical paths that raster back and forth into a target antiparallel-array arrangement.

We recently extended DNA origami to 3D nanoconstruction with a design strategy that can be conceptualized as stacking corrugated sheets of antiparallel helices (*19*). The resulting structures resemble bundles of double helices constrained to a honeycomb lattice (an example is shown in Fig. 1A; also see figs. S7 to S24 for detailed examples of how staple strands can be programmed to link the scaffold strand into an antiparallel array of honeycomb-pleated helices). The number, arrangement, and individual lengths of helices can be tuned to produce a variety of 3D shapes; we have developed a graphical software tool to aid in the design process (*20*). In this experiment, we expand the design space of accessible DNA-origami shapes to include a rich diversity of nanostructures with designed twist and curvature.

In our honeycomb-array framework, every double helix has up to three nearest neighbors (Fig. 1A) and is designed to connect to each by antiparallel strand crossovers, which are covalent phosphate linkages in the same form as that found in naturally occurring Holliday junctions. For explanatory purposes, here we assume that only staple strands, and not the scaffold strand, can cross over to form a Holliday junction between adjacent double helices (*19*). Every 7 base pairs (bp), the helical path of a strand rotates by 240°, assuming a B-form–DNA twist density of 10.5 bp per turn. Therefore, 14 bp gives rise to a rotation of 120° plus 360°, and 21 bp gives rise to a rotation of 0° plus two times 360°. As a result, antiparallel strand crossovers to one of the three nearest neighbors at 0°, 120°, and 240° can be engineered to occur once every 7 bp. Thus, along the helical axis of the whole honeycomb array, crossovers only can occur at positions that coincide with conceptual planes perpendicular to that axis spaced at 7-bp intervals.

These crossover planes can be used as a reference to conceive the honeycomb-pleated helix bundle as a 3D array of cells that by default each contain a 7-bp-long double-helical DNA fragment (Fig. 1B) that is mechanically coupled to its nearest neighbors. This abstraction of the DNA bundle as a collection of array cells is key for understanding how site-directed insertions and deletions of base pairs in the bundle can control twist and curvature.

We systematically adjusted the number of base pairs in selected subsets of array cells to realize DNA shapes that globally twist or bend along their helix-parallel axes. Because any array-cell DNA fragment is physically constrained by its neighbors in the honeycomb array, deletion of a base pair results in a local overwinding and tensile strain for that fragment, which causes it to exert a left-handed torque and a pull on its neighbors (Fig. 1C, top). The overwind strain can be relieved by a compensatory global left-handed twist of the bundle along its

---

[1]Department of Cancer Biology, Dana-Farber Cancer Institute, Boston, MA 02115, USA. [2]Department of Biological Chemistry and Molecular Pharmacology, Harvard Medical School, Boston, MA 02115, USA. [3]Wyss Institute for Biologically Inspired Engineering, Harvard University, Cambridge, MA 02138, USA.

*Present address: Physik Department and CiPSM, Technische Universität München, D-85748 Garching bei München, Germany.
†To whom correspondence should be addressed. E-mail: william_shih@dfci.harvard.edu

helix-parallel axis, whereas the tensile strain can be relieved by a compensatory global bend of the bundle toward that fragment along its helix-parallel axis. In the same way, insertion of a base pair into an array cell results in a local underwinding and compressive strain (Fig. 1C, bottom) that can be relieved by a compensatory global right-handed twist and bend away from the fragment along the helix-parallel axis.

Destructive cancellation of compensatory global bend deformations and constructive reinforcement of compensatory global twist deformations can be implemented, for example, by distribution of only deletions or only insertions in the bundle, as depicted in Fig. 1D. The bundle with only deletions is analogous to the architecture of protein coiled coils, where overwinding of right-handed α helices from 3.6 to 3.5 amino acids per turn, enforced by heptad-repeat phasing, is compensated by a global left-handed twist. Conversely, destructive cancellation of global twist deformations and constructive reinforcement of global bend deformations can be implemented, for example, by distribution of a gradient of deletions to insertions of base pairs through a bundle's cross section, as depicted in Fig. 1E. Steeper gradients of deletions to insertions can be implemented to achieve greater degrees of curvature.

To assess whether global twisting can be implemented, we chose as a model system a 10-row, 6-helix-per-row (10-by-6) bundle composed of 60 tightly interconnected DNA double helices (Fig. 2) that we previously had identified as a well-behaved folding architecture (*19*, *20*) and whose ribbonlike (as opposed to tubelike) structure makes observation of twisting more facile. We designed three versions of this bundle. In the default version that is designed not to twist, 19 crossover planes are spaced evenly in 7-bp steps across a length of 126 bp, or 12 complete turns at 10.5 bp per turn. We designed a second version of the 10-by-6 bundle in which we deleted a single base pair from every third array cell along each helix. Thus, one-third of all array cells contain overtwisted DNA fragments, resulting in a bundle with a length of 120 bp and an average twist density of 10 bp per turn. Additionally, we designed a third version of the 10-by-6 bundle in which we added a single base pair to every third array cell, resulting in a shape with a length of 132 bp and an average twist density of 11 bp per turn (see figs. S7 to S9 for design details).

The 10 by 6 bundles were folded by a two-step process. The first step involved initialization of the system by incubation at 80°C of the appropriate mixture of scaffold and staple strands in buffered solution. The second step involved gradual cooling of the strand suspension to room temperature. Next, the sample was subjected to agarose-gel electrophoresis. The fastest migrating band (excluding the free staple strands) typically represented the monomeric species. Thus, excision of this band from the gel, followed by recovery of the embedded particles by centrifugation through a cellulose-acetate filter, resulted in enrichment of well-folded particles. These gel-purified particles were then imaged by negative-stain transmission electron microscopy (TEM) (see note S1 for imaging methods and fig. S3 for additional zoom-out images). As previously reported, no systematic deformations were found in the default 10.5 bp per turn version of the bundle (Fig. 2A, bottom left) (*19*). However, particles designed with locally overtwisted DNA (Fig. 2B, bottom left) or locally undertwisted DNA (Fig. 2C, bottom left) appear to exhibit a global twist deformation when oriented so that they are viewed down the helical-axis interface or down the six-helix-wide side. The deformed appearance is not obvious for particles that are oriented with the 10-helix-wide side oriented parallel to the grid surface. Surprisingly, the 11 bp per turn designed twist density improved overall folding quality (Fig. 2F) of the 10-by-6 bundle. We speculate that the increased spacing between crossover planes may allow greater electrostatic-repulsion–driven bowing out of helices that, therefore, is easier to achieve. An alternative speculative explanation derives from the observation that, for helices surrounded by three neighbors in the honeycomb array, crossovers occur every 7 bp. An increased spacing of 8 bp may improve stability of these segments in a manner that affects the rate-limiting steps for folding. Systematic experiments in the future will be required for elucidating the determinants of folding speed and quality.

To verify the apparent twist, we separately polymerized each of the 10-by-6 bundle versions along the helical axes to form ribbons. When made up of bundles designed with only default 7-bp array cells, the resulting ribbons appeared to be completely straight with no detectable global twist (Fig. 2A, top right). In contrast, for both the versions with locally overtwisted and locally undertwisted DNA fragments, we consistently observed ribbons that clearly twist (see fig. S3 for additional zoom-out image data). To determine the chirality of these twisted ribbons, we collected tilt-pair images by rotating the TEM goniometer

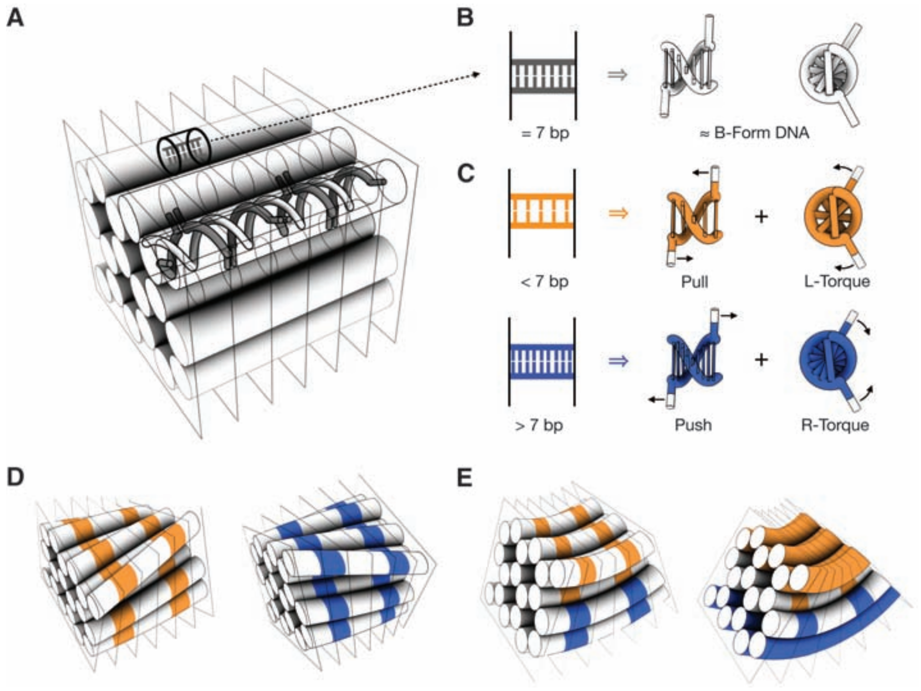

Fig. 1. Design principles for controlling twist and curvature in DNA bundles. (**A**) Double helices are constrained to a honeycomb arrangement by staple-strand crossovers. Semi-transparent crossover planes mark the locations of strand crossovers between neighboring helices, which are spaced at 7-bp intervals along the helical axis. From left to right, each plane contains a class of crossovers rotated in-plane by 240° clockwise with respect to the preceding plane. The crossover planes divide the bundle conceptually into helix fragments that can be viewed as residing in array cells (one cell is highlighted). (**B**) Array cell with default content of 7 bp, which exerts no stress on its neighbors. (**C**) Above, array cell with content of 5 bp, which is under strain and therefore exerts a left-handed torque and a pull on its neighbors. Below, array cell with content of 9 bp, which is under strain and therefore exerts a right-handed torque and a push on its neighbors. Force vectors are shown on only two of the four strand ends of the array-cell fragment for clarity. (**D**) (Left) Site-directed deletions installed in selected array cells indicated in orange result in global left-handed twisting with cancellation of compensatory global bend contributions; (right) site-directed insertions in selected array cells (shown in blue) result in global right-handed twisting. (**E**) Site-directed base-pair deletions (indicated in orange) and base-pair insertions (indicated in blue) can be combined to induce tunable global bending of the DNA bundle with cancellation of compensatory global twist contributions.

(Fig. 2, D and E). For ribbons polymerized from bundles with locally undertwisted DNA, we observed that the nodes consistently moved upward on an 80° counterclockwise sample-plane rotation. The experimental geometry (Fig. 2D, bottom) provides an unequivocal identification of the global twist as right-handed. Conversely, for ribbons constructed from bundles with locally overtwisted DNA, we observed that the ribbon nodes consistently moved downward on the same sample rotation, thus revealing a global left-handed twist.

We quantified the twist frequency by measuring the distance between consecutive nodes for multiple ribbons (Fig. 2G) and then plotting global twist per turn as observed for each version of the 10-by-6 bundles versus initially imposed double-helical twist density (Fig. 2H). Different architectures probably will exhibit global twisting that will vary in absolute magnitude but not in sign from the values observed for the 10-by 6-bundle because of differences in resistance to torsion as a function of cross-sectional shape. For example, a 60-helix bundle with a more extended cross section (e.g., 30 by 2 helices) would be expected to exhibit more global twist at the same initially imposed local double-helical twist density due to the lower torsional stiffness. We also experimentally observed global twist for a 3-by-6 bundle architecture, but because of the squarelike cross section, it was difficult to determine the location of the nodes and thereby quantify the magnitude of twisting.

These results imply that average double-helical twist density must be carefully considered during DNA-nanostructure design to avoid unwanted global twist deformations. Global twisting has been observed for DNA nanotubes assembled from oligonucleotide-based tiles with double-helical twist densities deviating from 10.5 bp per turn (*21*, *22*). Planar DNA origami (*18*) has been designed with an average twist density of 10.67 bp per turn. Intrinsic global twist of such designs as exists in solution, however, might not be obvious from image analysis of particles flattened by adhesion to surfaces.

We next explored the use of balanced gradients of insertions and deletions to produce global bend with no global twist by constructing seven versions of a three row, six-helix-per-row (3-by-6) bundle (Fig. 3A). The design contains 61 crossover planes evenly spaced along the helical axis. Between 15 crossover planes in the middle of the bundle, we implemented gradients of insertions and deletions across the short axis of the cross section (red segment in the models in Fig. 3, A to G; see figs. S10 to S18 for design details). We implemented increasingly steep gradients (Fig. 3H and figs. S10 to S18) up to extreme deviations from native B-form–DNA twist density, where one side of the 3-by-6 bundle has an average twist density of only 6 bp per turn, whereas the opposite side has a twist density as high as 15 bp per turn. We used a toy model that considers DNA as a continuum rod with elastic bending, stretch-compression, and twist-stretch coupling (see note S2 and fig. S1) and an iterative refinement procedure to identify gradients that produce bend angles from 30° to 180° in 30° steps with radii of curvature ranging from 64 to 6 nm.

Folding of five of the seven 3-by-6 bundle versions resulted in products that migrate as

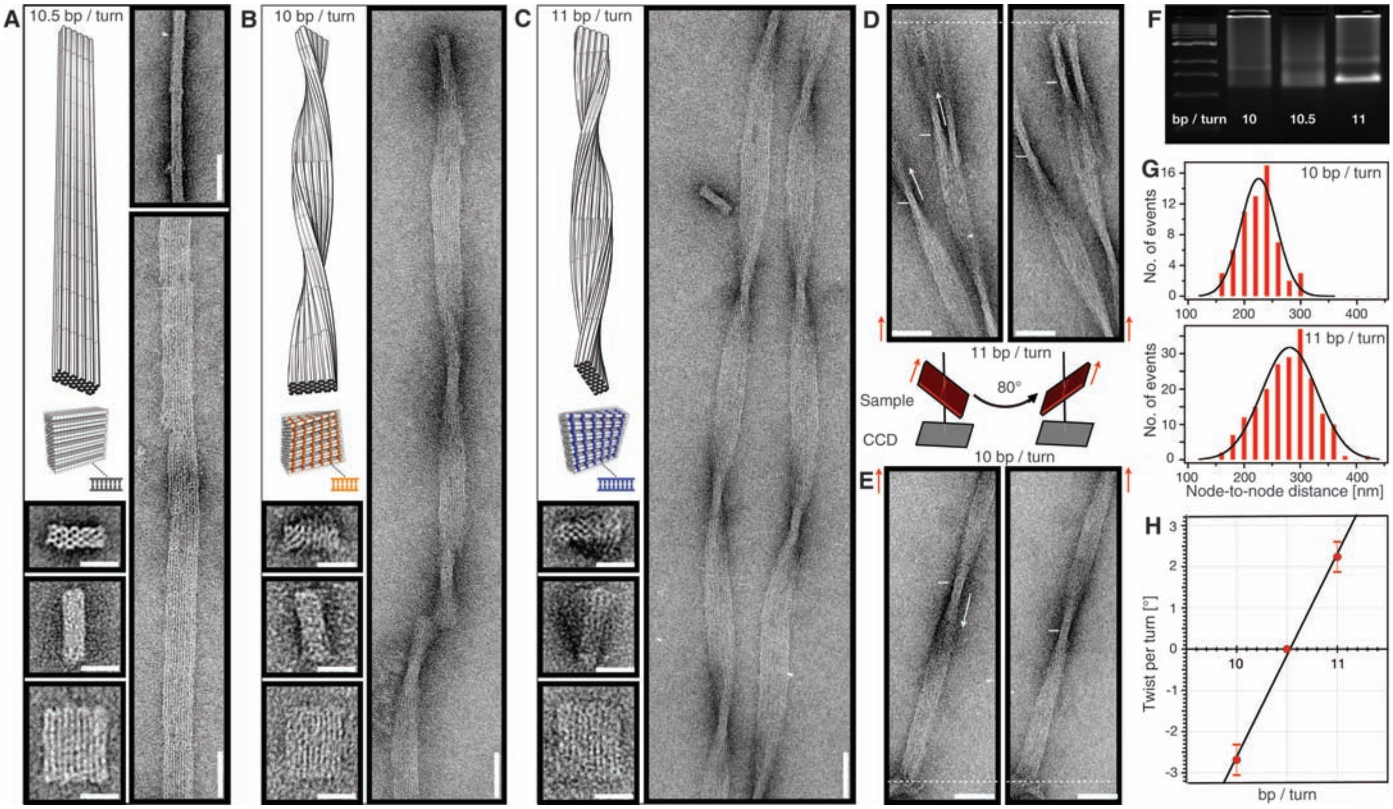

Fig. 2. Deviations from 10.5 bp per turn twist density induce global twisting. (**A** to **C**) (Top left) Models of a 10-by-6–helix DNA bundle (red) with 10.5, 10, and 11 bp per turn average double-helical twist density, respectively, and models of ribbons when polymerized (silver). (Bottom left) Monomeric particles as observed by negative-stain TEM. Scale bars, 20 nm. (Right) Polymeric ribbons as observed by TEM. Scale bars, 50 nm. (**D** and **E**) Tilt-pair images of twisted ribbons polymerized from 11 bp per turn (D) and 10 bp per turn (E); 10-by-6–helix bundles, recorded at goniometer angles of 40° and –40°. Arrows indicate the observed upward (for 11 bp per turn) or downward (for 10 bp/turn) direction of movement of the twisted-ribbon nodes. The dashed line provides a reference point (ends of ribbons remain stationary on goniometer rotation). CCD, charge-coupled device. (**F**) Ethidium-bromide–stained 2% agarose gel, comparing migration of unpurified folded bundles. (**G**) Histograms of the observed node-to-node distance in twisted ribbons, as observed in negative-stain TEM micrographs. Left- and right-handed ribbons undergo half-turns every 235 ± 32 nm (*n* = 62 internode distances measured) and 286 ± 48 nm (*n* = 197), respectively (numbers after the ± sign indicate SD). (**H**) Plot of observed global compensatory twist per turn versus double-helical twist density initially imposed by design. A value of 0.335 nm per bp was used to calculate global twist per turn from values obtained in (G). Error bars indicate SD.

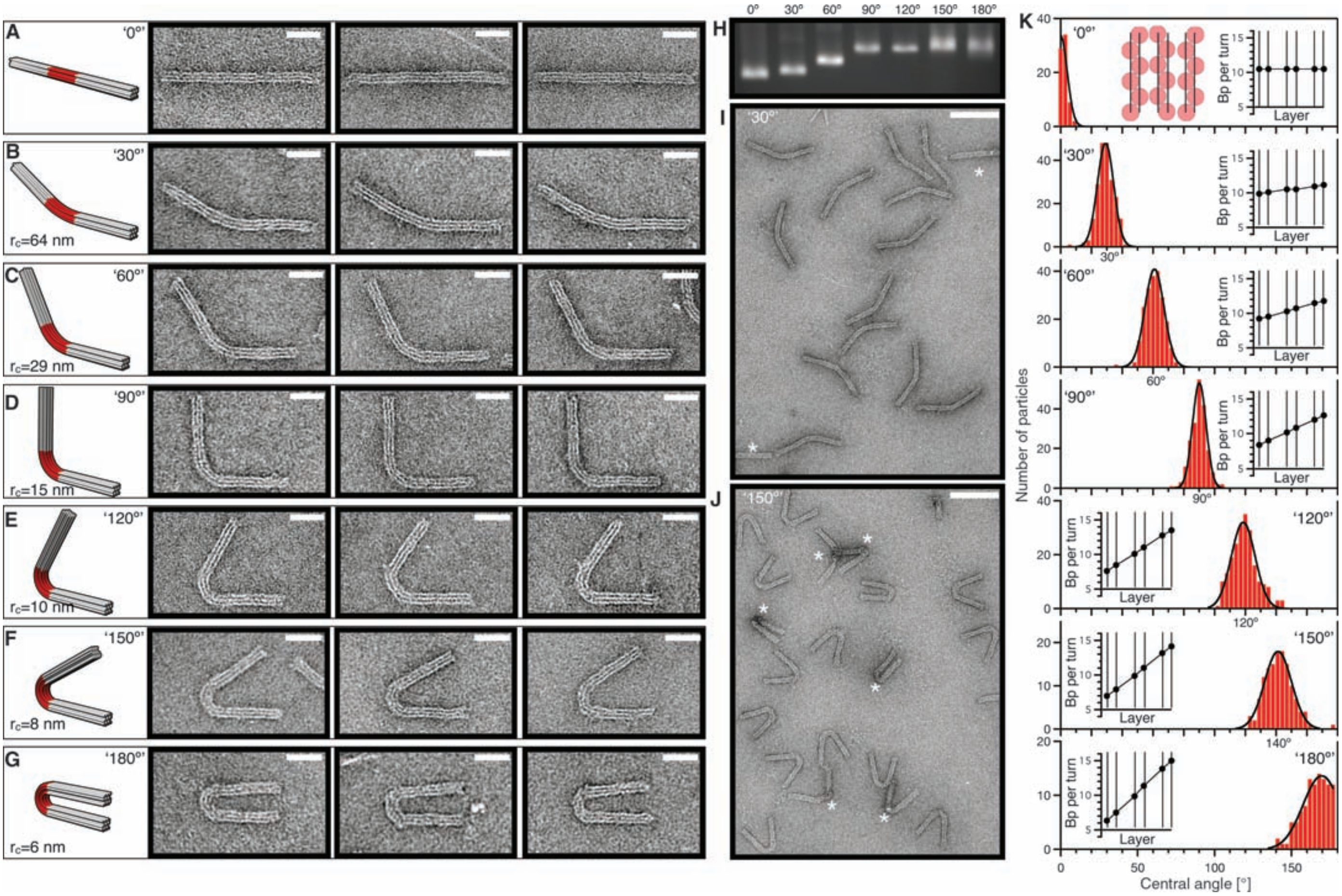

Fig. 3. Combining site-directed insertions and deletions induces globally bent shapes. (**A** to **G**) Models of seven 3-by-6–helix-bundle versions programmed to different degrees of bending and typical particles, as observed by negative-stain TEM. r_c, radius of curvature. Scale bars, 20 nm. (**H**) Ethidium-bromide–stained 2% agarose gel comparing migration of unpurified folding products of the seven differently bent bundles. (**I** and **J**) Low-magnification TEM micrographs of the bundle versions programmed to bend by 30° and 150°, respectively. Asterisks indicate defective particles, identified by the lack of three well-defined stripes at the bend. Scale bars, 100 nm. (**K**) Histograms of bend angles as observed in individual particles for the seven different bundle versions. Average bend angles were determined to be 0° ± 3° (*n* = 74), 30.7° ± 5.4° (*n* = 212), 62.4° ± 5.9° (*n* = 208), 91.3° ± 5.2° (*n* = 206), 121° ± 8.4° (*n* = 212), 143.4° ± 9° (*n* = 131), and 166° ± 9° (*n* = 106) (numbers after the ± sign indicate SD). (Insets) Plots of average double-helical twist density through the cross section of the bent segment that results from the pattern of insertions and deletions installed to induce bending.

sharp bands on a 2% agarose gel (Fig. 3H), indicating folding into an overall homogeneous shape, whereas the 150° and 180° versions migrate as more fuzzy bands, which suggests that a greater degree of shape heterogeneity is present. The latter two versions coincide with the two steepest insertion/deletion gradients. Such stark deviations from B-form DNA twist density apparently compromise folding quality and increase the frequency of defective particles. Moreover, the gel mobility decreases with increasing gradient of insertions and deletions, indicating pronounced changes in the aspect ratio of the particles.

We used negative-stain TEM to study the appearance of the particles (Fig. 3, A to G). The particles mainly adsorbed in two orientations on the TEM grids and exhibited a smooth appearance when oriented with the long axis of the bundle cross section parallel to the grid, but exhibited three pronounced stripes when oriented with the short axis parallel to the TEM grid (see note S4 and fig. S2 for a more detailed explanation of the origin of the stripes, as well as fig. S4 for image data with multiple particle orientations). The orientation giving rise to the "stripy" appearance allows for a direct assessment of the extent of the induced bending.

Bend angles ranging from 30° to 180°, as well as sharply bent radii of curvature down to 6 nm, close to the extreme bending of DNA found in the nucleosome (*23*), could be realized. Figure 3, I and J, gives a sense of the shape homogeneity exemplified by two bundle versions designed to bend at 30° and 150°, respectively. Additional zoom-out image data for each version of the 3-by-6 helix bundles is provided in fig. S4.

We quantified the distribution of bend angles for each version in the series of bundles. To avoid bias from obviously defective particles, we analyzed only those where three pronounced stripes were clearly discernible along the entire length. As an example, particles marked with an asterisk in Fig. 3, I and J, do not satisfy that criterion. We observed that the fraction of particles that failed this criterion was ~50% for radii of curvature above 10 nm but increased as a function of tightness of radii of curvature above 10 nm (fig. S4). Histograms of bend angles observed for the seven different 3-by-6 bundle versions are shown in Fig. 3K. The distributions each have a half-width at half maximum of 5° to 9°. Our toy model predicts thermally induced angular fluctuations with a SD from the mean bend angle of ~2.5° (see note S2 and fig. S1). The discrepancy between expected and observed distribution widths may be due to defects. Defective helices confer bending "individuality" to each particle, because defects change the effective gradient of insertions and deletions, as well as the compliance of a defective helix in the bundle. A future challenge will be to improve folding quality so that thermal fluctuations alone determine the angular precision of any produced shape. Our toy model can identify insertion and deletion patterns to an accuracy of 3° for desired mean bend angles less than or equal to 120°, although changes in environmental conditions may require adjustment of

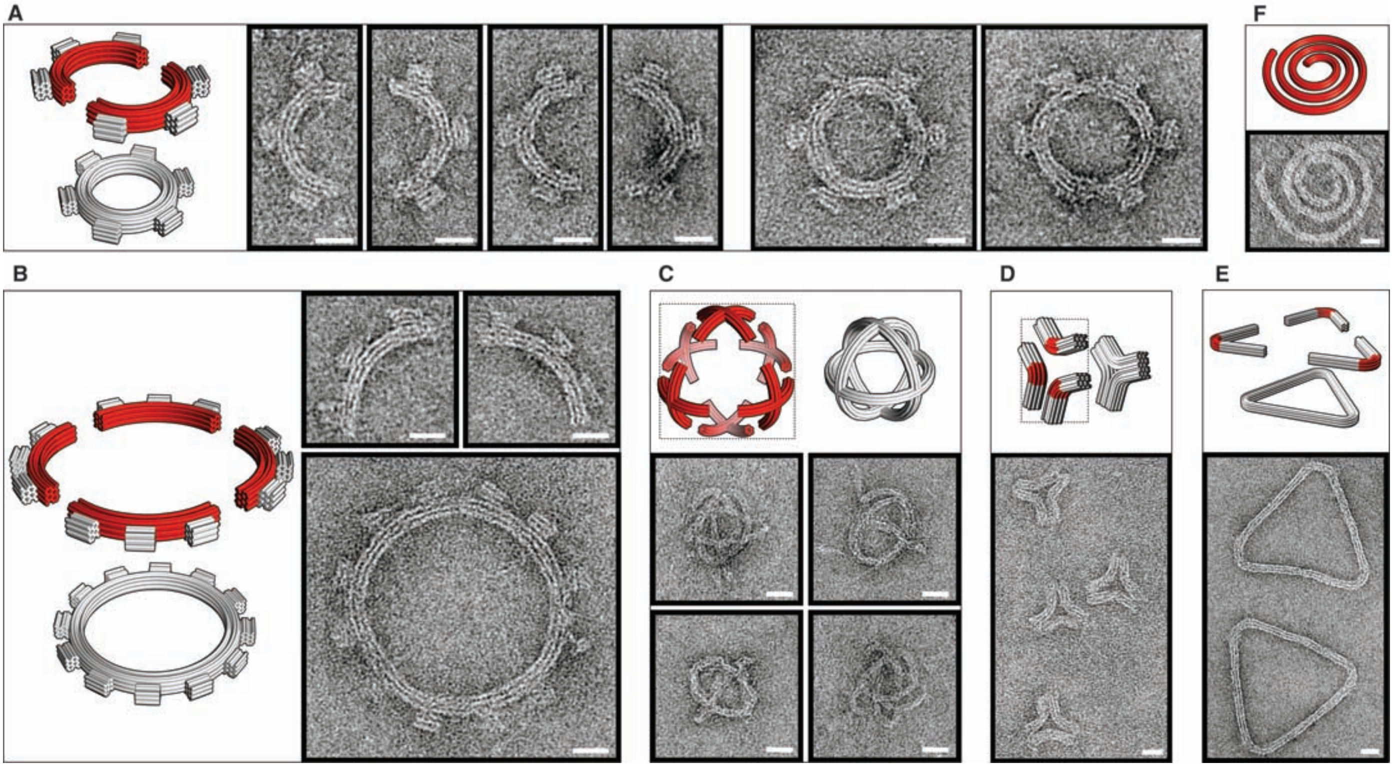

Fig. 4. Bending enables the design of intricate nonlinear shapes. Red segments indicate regions in which deletions and insertions are installed. Scale bars, 20 nm. (**A**) Model of a 3-by-6–helix DNA-origami bundle designed to bend into a half-circle with a 25-nm radius that bears three non-bent teeth. Monomers were folded in separate chambers, purified, and mixed with connector staple strands to form six-tooth gears. Typical monomer and dimer particles visualized by negative-stain TEM. (**B**) 3-by-6–helix bundle as in (A), modified to bend into a quarter circle with a 50-nm radius. Hierarchical assembly of monomers yields 12-tooth gears. (**C**) A single scaffold strand designed to fold into a 50-nm-wide spherical wireframe capsule resembling a beach ball and four typical particles representing different projections of the beach ball. The design folds as six bent crosses (inset) connected on a single scaffold. (**D**) A concave triangle that is folded from a single scaffold strand. The design can be conceptualized as three 3-by-6 bundles with internal segments designed to bend by 60°. (**E**) A convex triangle assembled hierarchically from three 3-by-6 bundles designed with a 120° bend (Fig. 3E). (**F**) A six-helix bundle programmed with varying degrees of bending folds into a spiral-like object.

model parameters. We expect our method for generating DNA shapes with tunable bending to be generally applicable for a wide range of bundle cross-sectional architectures, as long as extreme deviations from canonical B-form DNA twist density (less than 6 bp per turn or more than 15 bp per turn) are avoided.

To illustrate the diversity of curved shapes now accessible, we designed a DNA bundle bearing three “teeth” that is programmed to fold into a half circle with a 25-nm radius (Fig. 4A; also see fig. S19 for design details and fig. S5 for additional zoom-out image data). Using hierarchical assembly, two of these bundles can be combined into a circular object that resembles a nanoscale gear with six teeth. The teeth exhibited a greater frequency of folding defects than the body, at a rate of about one defective tooth out of three, perhaps related to their small size (only 42 bp long per double helix). About one-third of multimeric complexes were observed to be the target cyclic dimers, versus noncyclic dimers and higher-order multimers. By adjusting the gradient of insertions and deletions, the bundle can be tuned to fold into a quarter circle with a 50-nm radius (Fig. 4B; see also fig. S20 for design details). By connecting four of these quarter circles, a gear with 12 teeth can be manufactured. In this case, only about a tenth of the multimeric complexes were observed to be the target cyclic tetramers. In the future, target cyclization may be improved for objects designed with taller interfaces that resist out-of-plane bending and that are more tolerant of folding defects.

3D spherical shapes can be created as well (Fig. 4C). We designed a 50-nm-wide spherical wireframe object that resembles a beach ball by programming six interconnected vertices, each composed of two crossed six-helix bundles, to bend so that a projection of the edges of an octahedron onto a circumscribing sphere is completed (see fig. S21 for design details). We further designed a concave and a convex triangle (Fig. 4, D and E; see figs. S22 and S23 for design details) and a spiral consisting of six segments of a six-helix bundle that are each programmed to bend into a half circle with increasing radii of curvature (Fig. 4F; see fig. S24 for design details). The convex triangle is designed as a hierarchically assembling homotrimer. For this design, about one-third of multimeric complexes were observed to be the target cyclic trimers (additional image data on all objects shown in Fig. 4 is provided in fig. S6).

Precisely arranged bent DNA and associated DNA-binding proteins play an important role in transcriptional regulation and genomic packaging (*24*–*26*). Programmable DNA bending might prove useful as a probe to study the propensity of such proteins to bind pre-bent DNA substrates and also to probe the propensity of different DNA sequences to adopt specifically bent conformations (*27*).

References and Notes

1. N. C. Seeman, *Nature* **421**, 427 (2003).
2. N. C. Seeman, *J. Theor. Biol.* **99**, 237 (1982).
3. T. J. Fu, N. C. Seeman, *Biochemistry* **32**, 3211 (1993).
4. X. J. Li *et al.*, *J. Am. Chem. Soc.* **118**, 6131 (1996).
5. E. Winfree *et al.*, *Nature* **394**, 539 (1998).
6. H. Yan, S. H. Park, G. Finkelstein, J. H. Reif, T. H. LaBean, *Science* **301**, 1882 (2003).
7. P. W. Rothemund *et al.*, *J. Am. Chem. Soc.* **126**, 16344 (2004).
8. F. Mathieu *et al.*, *Nano Lett.* **5**, 661 (2005).
9. S. M. Douglas, J. J. Chou, W. M. Shih, *Proc. Natl. Acad. Sci. U.S.A.* **104**, 6644 (2007).
10. D. Liu *et al.*, *Proc. Natl. Acad. Sci. U.S.A.* **101**, 717 (2004).
11. P. Yin *et al.*, *Science* **321**, 824 (2008).
12. R. P. Goodman *et al.*, *Science* **310**, 1661 (2005).
13. J. H. Chen, N. C. Seeman, *Nature* **350**, 631 (1991).
14. Y. Zhang, N. C. Seeman, *J. Am. Chem. Soc.* **116**, 1661 (1994).
15. Y. He *et al.*, *Nature* **452**, 198 (2008).
16. C. Zhang *et al.*, *Proc. Natl. Acad. Sci. U.S.A.* **105**, 10665 (2008).

17. W. M. Shih, J. D. Quispe, G. F. Joyce, *Nature* **427**, 618 (2004).
18. P. W. Rothemund, *Nature* **440**, 297 (2006).
19. S. M. Douglas *et al.*, *Nature* **459**, 414 (2009).
20. S. M. Douglas *et al.*, *Nucleic Acids Res.*; published online 16 June 2009 (10.1093/nar/gkp436).
21. J. C. Mitchell *et al.*, *J. Am. Chem. Soc.* **126**, 16342 (2004).
22. C. Lin *et al.*, *Nano Lett.* **9**, 433 (2009).
23. K. Luger *et al.*, *Nature* **389**, 251 (1997).
24. J. A. Borowiec *et al.*, *J. Mol. Biol.* **196**, 101 (1987).
25. J. Chang *et al.*, *Structure* **14**, 1073 (2006).
26. H. G. Garcia *et al.*, *Biopolymers* **85**, 115 (2007).
27. S. C. J. Parker, L. Hansen, H. O. Abaan, T. D. Tullius, E. H. Margulies, *Science* **324**, 389 (2009); published online 12 March 2009 (10.1126/science.1169050).

28. H.D. thanks Andres E. Leschziner for training in electron microscopy and generous supply of image processing hardware and software. This work was supported by Claudia Adams Barr Program Investigator, Wyss Institute for Biologically Inspired Engineering, and NIH New Innovator (1DP2OD004641-01) grants to W.M.S. and a Feodor-Lynen Humboldt Fellowship to H.D. H.D., S.M.D., and W.M.S. designed the research for this paper. H.D. developed rules for twisting and bending; H.D. and S.M.D. designed all shapes; H.D. and S.M.D. collected data; H.D. analyzed data; S.M.D. provided caDNAno software support; and H.D., W.M.S., and S.M.D. wrote the manuscript.

Supporting Online Material
www.sciencemag.org/cgi/content/full/325/5941/725/DC1
Materials and Methods
SOM Text
Figs. S1 to S26
References

30 March 2009; accepted 25 June 2009
10.1126/science.1174251

Unexpected Epoxide Formation in the Gas-Phase Photooxidation of Isoprene

Fabien Paulot,[1]* John D. Crounse,[2] Henrik G. Kjaergaard,[3,4] Andreas Kürten,[1]† Jason M. St. Clair,[1] John H. Seinfeld,[1,2] Paul O. Wennberg[1,5]

Emissions of nonmethane hydrocarbon compounds to the atmosphere from the biosphere exceed those from anthropogenic activity. Isoprene, a five-carbon diene, contributes more than 40% of these emissions. Once emitted to the atmosphere, isoprene is rapidly oxidized by the hydroxyl radical OH. We report here that under pristine conditions isoprene is oxidized primarily to hydroxyhydroperoxides. Further oxidation of these hydroxyhydroperoxides by OH leads efficiently to the formation of dihydroxyepoxides and OH reformation. Global simulations show an enormous flux—nearly 100 teragrams of carbon per year—of these epoxides to the atmosphere. The discovery of these highly soluble epoxides provides a missing link tying the gas-phase degradation of isoprene to the observed formation of organic aerosols.

Isoprene is the largest source of nonmethane hydrocarbons to the atmosphere (~500 Tg C/year) (*1*). It is produced by deciduous plants (*2*) and plays a critical role in tropospheric chemistry over large regions of the globe (*3*). In many forested regions, isoprene oxidation by OH occurs far from combustion of biomass and fossil fuel, so nitric oxide (NO) concentrations are very low. Many of the details of the chemical oxidation mechanism under these conditions remain to be elucidated, hindering assessment of the consequences of changes in isoprene emissions from land use and climate variation (*1*, *4*–*6*) or changes in NO emissions. In addition to the uncertainty in the gas-phase chemistry, there is no agreement on the mechanism involved in the formation of secondary organic aerosol (SOA) from isoprene oxidation (*7*).

Where NO is low, isoprene photooxidation is expected to yield the hydroxyhydroperoxides, ISOPOOH = β-ISOPOOH + δ-ISOPOOH (Reaction Series 1, A and B) (*8*, *9*). These series of reactions are expected to strongly depress the concentrations of OH and HO$_2$ (together known as HO$_x$) in regions with high isoprene emissions. Observed HO$_x$ levels remain, however, almost unchanged over a wide range of isoprene concentrations, inconsistent with the simulated influence of Reaction Series 1, A and B (*10*–*12*). Simulations and measurements of HO$_x$ have been partly reconciled with substitution of the speculative Reaction Series 1C, where formation of methacrolein (MACR) and formaldehyde is accompanied by OH formation, thus reducing the impact of isoprene on HO$_x$ levels (*11*).

Analogous to Reaction Series 1, A to C, addition of OH on the other double bond yields similar hydroxyhydroperoxides (β1- and δ1-ISOPOOH) and methylvinylketone (MVK) (*13*). Both unimolecular decomposition of the peroxy radical (*14*) and reaction with HO$_2$ (*15*) have been proposed in Reaction Series 1C. Although OH reformation (15 to 65%) has been measured for the reactions of HO$_2$ with acylperoxy and β-carbonyl peroxy radicals, low OH yields (<6%) have been reported from the reactions of HO$_2$ with β-hydroxy peroxy radicals, structurally more similar to isoprene peroxy radicals (*15*).

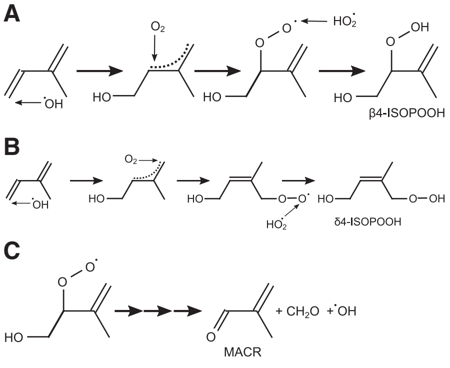

Reaction Series 1.

We show here that ISOPOOH is formed in large yields (>70%) via the channels shown in Reaction Series 1, A and B, with concomitant formation of MVK and MACR in much smaller yields (<30%) via the channel shown in Reaction Series 1C. The branching through Reaction Series 1C yields OH, although substantially less than required to close the HO$_x$ budget (*11*).

We show below that the oxidation of ISOPOOH by OH produces dihydroxyepoxides (IEPOX = β-IEPOX + δ-IEPOX). This HO$_x$ neutral mechanism produces IEPOX with yields exceeding 75% (Reaction Series 2, A and B). This mechanism is likely specific to isoprene and other polyalkenes. Analogous to liquid phase processes (*16*), it profoundly differs from gas-phase oxidation of simple alkenes by OH (e.g., Reaction Series 1, A and B), which would result in the formation of the dihydroxydihydroperoxides. Formation of these compounds is not observed in these experiments.

The gas-phase formation of IEPOX in high yields provides a suitable gas-phase precursor for Secondary Organic Aerosol from isoprene oxidation (*i*SOA) under low-NO$_x$ conditions (*17*–*19*) and may help resolve an outstanding puzzle in atmospheric aerosol chemistry. Although epoxides have previously been speculated as a possible precursor for *i*SOA (*17*), no mechanism was known to produce them in either the gas or aerosol phase. Consistent with expectation that IEPOX can serve as a precursor to *i*SOA, we

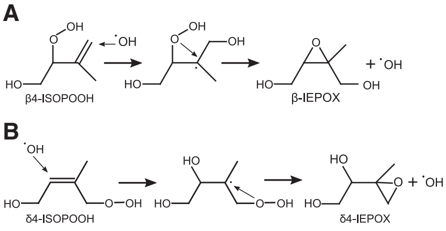

Reaction Series 2.

---

[1] Division of Engineering and Applied Science, California Institute of Technology, Pasadena, CA 91125, USA. [2] Division of Chemistry and Chemical Engineering, California Institute of Technology, Pasadena, CA 91125, USA. [3] Department of Chemistry, University of Otago, Dunedin, New Zealand. [4] Department of Chemistry, University of Copenhagen, Copenhagen, Denmark. [5] Division of Geological and Planetary Sciences, California Institute of Technology, Pasadena, CA 91125, USA.

*To whom correspondence should be addressed. E-mail: paulot@caltech.edu

†Present address: Institute for Atmospheric and Environmental Sciences, Goethe University, Frankfurt am Main, Germany.